ACS Energy LETTERS

http://pubs.acs.org/journal/aelccp

LETTER

Graphene Oxide Shells on Plasmonic Nanostructures Lead to High-Performance Photovoltaics: A Model Study Based on Dye-Sensitized Solar Cells

Yoon Hee Jang,[†,∥] Adila Rani,[†] Li Na Quan,[†,‡] Valerio Adinolfi,[‡] Pongsakorn Kanjanaboos,[‡,#] Olivier Ouellette,[‡] Taehwang Son,[§] Yu Jin Jang,[†] Kyungwha Chung,[†] Hannah Kwon,[†] Donghyun Kim,[§] Dong Ha Kim,[*,†] and Edward H. Sargent[*,‡]

[†]Department of Chemistry and Nano Science, Ewha Womans University, 52, Ewhayeodae-gil, Seodaemun-gu, Seoul 03760, South Korea

[‡]Department of Electrical and Computer Engineering, University of Toronto, 10 King's College Road, Toronto, Ontario M5S 3G4, Canada

[§]School of Electrical and Electronic Engineering, Yonsei University, 50, Yonsei-ro, Seodaemun-gu, Seoul 03722, South Korea

Supporting Information

ABSTRACT: **The incorporation of plasmonic nanoparticles (NPs) into photovoltaic devices can increase light absorption and in turn improve solar cell performance. The graphene oxide-encapsulated gold NPs (Au@GO NPs) are designed and incorporated into photoanodes to demonstrate plasmonic dye-sensitized solar cells. The coupling between GO and the Au NPs has the beneficial effect of extending solar spectral utilization in the long-wavelength portion of the visible spectrum. In addition, GO encapsulation reduces charge recombination on the surface of the NPs and facilitates improved charge transport. As a result, champion devices with plasmonic photoanodes containing Au@GO NPs deliver a power conversion efficiency that reaches 9.1%. This corresponds to an enhancement in photocurrent and power conversion efficiency of 19 and 17%, respectively, compared to control devices.**

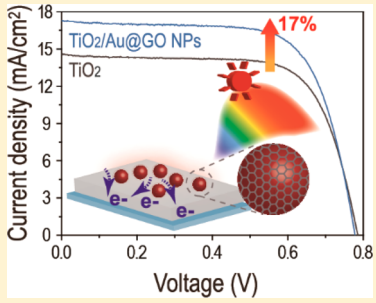

Plasmonic effects have been widely reported as a solution to overcome the limited light absorption of thin film photovoltaic devices.[1−6] To date, the development of plasmonic photovoltaics has been based on diverse enhancement mechanisms. Near-field enhancement by locally enhanced surface-plasmon excitation of metal nanoparticles (NPs) is a representative route to increase the light absorption cross section of photoactive materials.[7−10] In addition, far-field scattering effects by relatively large NPs can increase the optical path length by effectively reflecting light into solar cells.[11−14] Another possible route is plasmon-induced charge carrier generation directly participating in photocurrent generation.[15−17] These plasmonic contributions were shown to have a beneficial effect in diverse photovoltaic systems, particularly dye-sensitized solar cells (DSSCs), in which the number of photons absorbed by sensitized dye molecules can notably increase through the incorporation of plasmonic NPs.[7,8,15,18−26]

In a seminal investigation of the applicability of plasmon resonance effects in DSSCs, Ag NPs were deposited on TiO_2 films, resulting in improvement of the optical absorption of the dye due to Ag plasmon resonance.[20] In 2008, Hägglund et al. observed that the LSPR of elliptical Au disks enhanced the charge carrier generation rate in the dye.[21] Since then, several studies have been conducted, and still more efforts are underway to further increase power conversion efficiencies (PCEs) by introducing properly designed plasmonic structures into DSSCs. To the best of our knowledge, the plasmonic DSSCs presenting the greatest increase in PCEs were augmented with small Au NPs (~2 nm in size) in a TiO_2 photoanode, enhancing the efficiency by 84%.[22] In that study, it was shown that improving photovoltage by a negative shift of the quasi-Fermi level of a Au-inlaid TiO_2 composite, as well as increasing dye excitation by plasmon resonance of the Au NPs, played a major role in achieving high-efficiency DSSCs. Hammond and Belcher demonstrated wide-spectrum DSSCs using multiple core−shell plasmonic structures and achieved a PCE of 10.8%, which represents the highest value among reported plasmonic DSSCs to date.[23] In this case, efficiency was

Received: November 17, 2016
Accepted: December 5, 2016
Published: December 5, 2016

DOI: 10.1021/acsenergylett.6b00612
ACS Energy Lett. 2017, 2, 117−123

maximized when light harvesting was balanced between photoabsorption within the dye and localized surface plasmon resonance (LSPR) of tailored plasmonic NPs.

Graphene-based materials have been applied to photovoltaic devices in various ways, which contributed to marked improvements in charge transport properties.[27−31] Yang et al. reported two-dimensional graphene layers introduced into the TiO_2 electrodes of DSSCs that functioned as bridges between TiO_2 NPs to bring faster electron transport and lower recombination.[28] The back-transport reaction resulting from direct contact between the electrolyte and fluorine-doped tin oxide (FTO) was effectively suppressed by configuring the graphene−TiO_2 nanocomposite interfacial layer between FTO and the TiO_2 electrode.[27] Yang et al. demonstrated graphene oxide (GO) having a higher work function (5.2 eV) as an efficient hole transporting layer in organic solar cells.[29] Most recently, nanocomposites of graphene/TiO_2 were applied as the electron collection layer in perovskite-based solar cells. Charge collection in the nanocomposites was superiorly improved by virtue of the graphene nanoflakes.[30]

Taking note of the above observations, optimizing the configuration of plasmonic NPs may be a crucial factor in increasing light collection in DSSCs. Thus, in this work, we designed GO-encapsulated Au NPs (Au@GO NPs) and configured a stable plasmonic photoanode to maximize the photocurrent and efficiency of a ruthenium-dye-sensitized TiO_2-based solar cell. Au@GO NPs showed remarkably enhanced absorption properties in the long-wavelength portion of the visible spectrum (600−800 nm), as well as surface plasmon features, allowing broad-band light harvesting. Furthermore, the GO thin shell played an important role in the improvement of charge transport by suppressing charge recombination. The origin and mechanism of the plasmonic enhancements were investigated by conductivity measurements, electrochemical impedance spectroscopy (EIS), and intensity-modulated photocurrent/photovoltage spectroscopy (IMPS/IMVS).

Au@GO NP Characterization. Thin layers of GO were attached to the surface of Au NPs through the electrostatic interaction between Au NPs and GO sheets. First, to cover the citrate-capped Au NPs' surface with GO, positively charged GO suspensions were synthesized. According to the modified Hummer method, the oxidation of graphite in an acidic medium and the following exfoliation of graphitic oxide attached a chemical functional group, for example, carboxylic acid (COOH), onto the surface of GO sheets, resulting in negatively charged GO ($GO\text{-}COO^-$).[32] Subsequently, the surface functional carboxylic acids were activated by *N*-ethyl-*N*′-(3-dimethyl aminopropyl)carbodiimide (EDC) and reacted with ethylenediamine (or triethylamine). Amine groups (NH_2) were introduced on the surface of the GO, and positively charged GO ($GO\text{-}NH_3^+$) suspensions were obtained. These positively charged GO sheets were characterized using X-ray photoelectron spectroscopy (XPS), UV−vis absorption, and zeta (ζ)-potential analysis. As shown in the XPS survey spectra (Figure S1a,b, Supporting Information), the N 1s peak at 400 eV was observed only in the case of positively charged GO due to the presence of the surface amine groups of $GO\text{-}NH_3^+$. To provide further evidence of formation of $GO\text{-}NH_3^+$, the C 1s peak was deconvoluted using a Gaussian fitting model. The high-resolution C 1s spectrum of initially synthesized $GO\text{-}COO^-$ (Figure S1c, Supporting Information) clearly showed carbon species in different functional groups, that is, sp^2 and sp^3 hybridized carbons in an aromatic ring (C═C, 284.0 eV; C−C, 284.8 eV), epoxy or hydroxy (C−O, 286.8 eV), carbonyl (C═O, 288.2 eV), and carboxylate (O−C═O, 289.0 eV). Meanwhile, additional components at 286.0 and 287.5 eV corresponding to carbon in C−N and O═C−N bonds, respectively, were observed, which confirms the successful NH_2 functionalization (Figure S1d, Supporting Information).

The initial negatively charged GO suspension in DI water exhibits an absorption band at ∼230 nm and a weak shoulder at ∼300 nm, attributed to the $\pi-\pi^*$ and $n-\pi^*$ transitions of the C═C and C═O bonds, respectively.[33] During the reaction between negatively charged GO and ethylenediamine with EDC, a hypsochromic shift in the peak of the $\pi-\pi^*$ transitions was observed, as seen in the UV−vis measurement (Figure S1e, Supporting Information); this is explained by the dissociation of oxygen-containing functional groups of GO, including carboxyl groups and aromatic hydroxyl groups.[34] Additionally, ζ-potential values of GO suspensions further support the formation of surface functional groups, indicating the positive characteristic of amine functional groups on GO (Figure S1f, Supporting Information).

Electrostatic interactions caused citrate-capped Au NPs to be covered by $GO\text{-}NH_3^+$ sheets (Figure 1a). As shown in the TEM

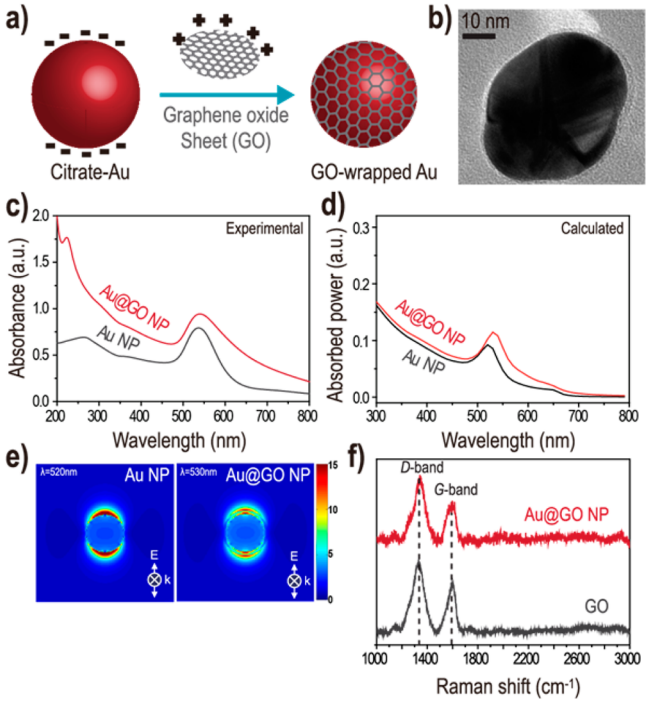

Figure 1. Characterization of Au@GO NPs. (a) Schematic illustration of the GO-wrapped Au NPs synthesis process. (b) TEM image of Au@GO NPs. (c) Experimental and (d) calculated UV−vis absorption spectra of Au NPs and Au@GO NPs. (e) Normalized electric field intensity distribution calculated by the FDTD simulation of Au NPs and Au@GO NPs. (f) Normalized Raman spectra of GO and Au@GO NPs.

image (Figures 1b and S2, Supporting Information), the obtained Au NPs are elliptical in shape with a diameter of 50−60 nm along the long axis. In addition, rough and crinkled features associated with flexible and ultrathin GO sheets can be clearly observed on the surface of the Au NPs, indicating a GO shell thickness of 4−5 nm. During the synthesis procedure, the overall structure or morphology of Au NPs was not altered,

DOI: 10.1021/acsenergylett.6b00612
ACS Energy Lett. 2017, 2, 117−123

except for the formation of a thin GO shell on the surface of Au NPs (Figure S2, Supporting Information).

The optical properties of the as-synthesized Au NPs and Au@GO NPs were then investigated. A noticeable difference in the UV−vis absorption spectra of the Au NPs with and without a GO shell is evident in Figure 1c. The position of the LSPR band of Au NPs is sensitive to the change in the surrounding medium. Therefore, the broadening and red shift of the LSPR band at ∼520 nm was attributed to the presence of a thin GO shell. In addition, the overall absorption in the whole spectral range was enhanced after GO coating. The characteristic absorption peak of GO is also present at ∼230 nm. The total absorbed power (Figure 1d) was calculated based on the three-dimensional finite-difference time domain (FDTD) method, and the result coincides with the experimental spectrum. The calculated electromagnetic intensity profiles at the resonance wavelengths of Au NPs (520 nm) and Au@GO NPs (530 nm) are displayed in Figure 1e. The electric field around Au@GO is diminished compared to that for Au NPs, most likely because of the shielding effect of the GO shell.

The presence of the GO shell was further confirmed by Raman spectroscopy. Figure 1f shows the Raman spectra of positively charged GO and Au@GO NPs under 633 nm excitation. In the Raman spectrum of graphene, D and G bands are usually observed. The D band at ∼1350 cm^{-1} is derived from the structural defects of graphite (the A_{1g} symmetry mode). The first-order scattering of the E_{2g} mode of sp^2 carbon atoms in graphene gives rise to a peak at ∼1580 cm^{-1}, named the G band.[35,36] The Raman spectrum of GO-NH_3^+ exhibits both the D and G bands at ∼1337 and ∼1595 cm^{-1}, respectively. The intensity of the D band was even higher than that of the G band. The 2D peak (i.e., overtone of the D band at ∼2700 cm^{-1}) was not revealed due to significant structural disorder or defects arising from the harsh oxidation synthesis process.[37,38] After the encapsulation of GO, two characteristic peaks were still present, and the D and G band positions remained the same.

Fabrication of Plasmonic DSSCs and Device Performance. Plasmonic photoanodes inlaid with GO-encapsulated Au NPs were fabricated following the overall procedure depicted in Figure 2a. First, a TiO_2 film was deposited on a FTO substrate by the doctor-blade method and crystallized by high-temperature sintering. Then, to ensure the chemical interaction between TiO_2 and Au@GO NPs, the TiO_2 film was modified with 3-aminopropyltriethoxysiliane (APTES). Even after the as-synthesized GO was functionalized with amine groups, surface functional OH groups partially remained on the surface of GO, which could interact with APTES. The APTES-modified TiO_2 film was finally immersed in the as-prepared Au@GO NP colloidal solution and washed with DI water to remove the unbound NPs. The SEM images in Figure 2b show the fabricated plasmonic photoanodes where discrete Au NPs were well distributed on the surface of TiO_2 without any noticeable agglomeration. However, partial agglomeration of Au@GO NPs was observed, which may result from the multiple synthetic steps to form GO shells.

The amount of incorporated NPs was tuned simply by controlling the immersion time of APTES-modified TiO_2 films into the NPs' colloidal solution. With increasing immersion time, the amount of NPs deposited was gradually increased, which was verified through a series of SEM images (Figure S3, Supporting Information). The performance of devices with varying amounts of NPs was investigated first, and the results are displayed in Figure S4 and Table S1, Supporting Information. With short dipping times (less than 30 min), only a slight improvement was observed (results not shown) due to insufficient incorporation of NPs. The best performance was obtained in both types of devices (with Au and Au@GO NPs) with a dipping time of 30 min, after which the PCE gradually decreased with the increasing amount of plasmonic NPs on TiO_2 films, suggesting that the presence of Au NPs in too large amounts could cause undesirable effects such as increased charge carrier recombination. The performance of the champion solar cell with the optimal amount of plasmonic NPs is shown in Figure 3a and listed in Table 1 (the average cell performance with variation is indicated in Figure S5 and Table S2, Supporting Information). Interestingly, while both the open-circuit voltage (V_{oc}) and fill factor (FF) remained unaffected, the photocurrent was greatly enhanced by the

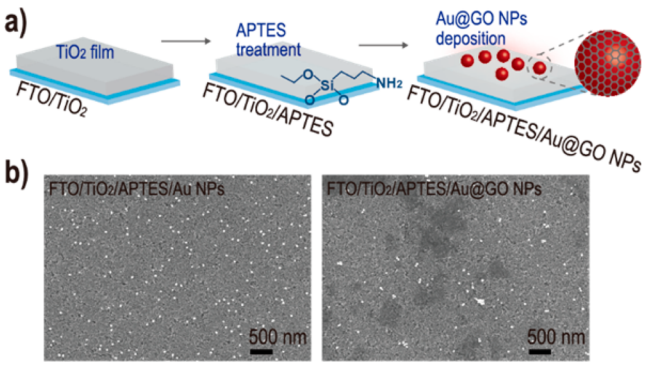

Figure 2. (a) Schematic describing the fabrication of the plasmonic photoanodes. (b) SEM images of plasmonic photoanodes configured with (left) FTO/TiO_2/APTES/Au NPs and (right) FTO/TiO_2/APTES/Au@GO NPs.

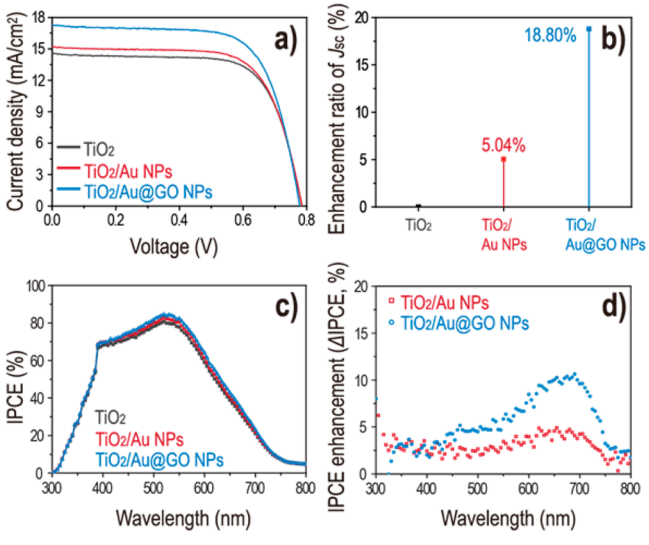

Figure 3. (a) Photocurrent density−voltage (J−V) characteristic of the control and plasmonic champion DSSCs with Au NPs and Au@GO NPs. (b) Corresponding enhancement ratio of the current density over the control device. (c) Incident photon-to-current conversion efficiency (IPCE, %) curves of control and plasmonic DSSCs with Au NPs and Au@GO NPs. (d) IPCE enhancement (ΔIPCE (%)) of plasmonic DSSCs with Au NPs and Au@GO NPs over the control device.

DOI: 10.1021/acsenergylett.6b00612
ACS Energy Lett. 2017, 2, 117−123

Table 1. Photovoltaic Parameters for the Best Performance Cell of Control and Plasmonic DSSCs with Au and Au@GO NPs at a Dipping Time of 30 min

photoanode types[a]	V_{oc} [V]	J_{sc} [mA/cm^2]	FF	η [%]	R_2 [Ω][b]	T_e [ms][c]
TiO_2	0.787	14.47	0.682	7.77	99.99	5.04
TiO_2/Au NPs	0.788	15.20	0.664	7.95	77.41	5.70
TiO_2/Au@GO NPs	0.780	17.19	0.676	9.06	70.98	6.37

[a]Control and plasmonic photoanodes with Au and Au@GO NPs. [b]Charge transport resistance. [c]Electron lifetime ($\tau_e = 1/(2\pi f_{mid})$) calculated from the EIS results.

introduction of plasmonic NPs, the leading cause of the enhancement in efficiency. Short-circuit current (J_{sc}) values are compared in Figure 3b, in which the improvement in plasmonic cells is apparent. A remarkably enhanced J_{sc} of 17.19 mA·cm^{-2} was obtained from the cell containing Au@GO NPs under optimal conditions, corresponding to an increase of ∼18.8% with respect to the control device (without the plasmonic NPs). In contrast, plasmonic cells without GO wrapping showed a J_{sc} of 15.2 mA·cm^{-2}, which was ∼13.1% lower than that of the plasmonic cell with GO wrapping. Considering the overall device performance, the outer, thin GO shell plays a significant role in enhancing the optical and electrical properties of plasmonic solar cells. We further investigated the mechanism of performance enhancement of the plasmonic solar cells with optimal Au@GO NPs by performing optical and electrical characterization.

Optical and Electrical Characterization. To investigate the origin of the performance enhancement by optical effects, the incident photon-to-current conversion efficiency (IPCE) spectra were measured for devices with and without plasmonic photoanodes (Figure 3c), which was obtained from a different set of cells than those reported in Table 1. In comparison with the control device (without plasmonic NPs), the IPCE spectra of the plasmonic devices showed increased values over the entire wavelength range. Furthermore, the device with Au@GO NPs exhibits a higher IPCE value than the one with Au NPs. The enhancement in the IPCE (ΔIPCE, %) was subsequently calculated and is displayed in Figure 3d. A broadly distributed enhancement is observed from 400 to 800 nm for both plasmonic devices, and strong enhancement was achieved from 600 to 700 nm for the devices containing Au@GO NPs. The notable enhancement in IPCE, especially in longer-wavelength regions, is attributed to broad-band light absorption by GO-encapsulated Au NPs, as shown in the UV−vis absorption profile of Au@GO NPs. However, IPCE enhancement does not follow the LSPR band at ∼540 nm.

To address the contribution of plasmonic effects to the improved device performance, scanning kelvin probe microscopy (SKPM) was performed, providing information about surface potential changes of TiO_2 by injection of hot electrons from plasmon decay of Au NPs to trap sites in the conduction band of TiO_2.[39] The samples were excited under a xenon light source for 380 s, and the surface potential changes were recorded. No significant differences in the work function were observed, that is, the surface potential between TiO_2 and the TiO_2/Au@GO NPs film remained the same (Figure S6, Supporting Information). On the basis of the IPCE and SKPM results, we can conclude that the solar cell efficiency increased primarily through broad-band light absorption by Au@GO NPs, whereas plasmonic effects, such as LSPR-induced charge injection or near-field enhancement, played a minor role in the performance enhancement. In addition to the enhancement of light-harvesting capability by synergistic coupling of Au NPs and the GO shell, the performance improvement may result from enhanced charge transport and reduced recombination effects.

To corroborate these potential impacts on the electrical properties, conductivity, EIS, and IMPS/IMVS measurements were performed. We examined the electronic transport properties of the prepared photoanodes by performing conductivity measurements on films kept in the dark. For this measurement, a symmetric film was constructed with the hole extracting contact layers (MoO_3/Au/Ag) on top of the photoanode films. The plasmonic photoanodes (FTO/TiO_2/Au or Au@GO NPs) showed higher conductivity than the photoanode without plasmonic NPs (FTO/TiO_2), in which the conductivity was obtained from the slope of the current density−(voltage/thickness) curves (Figure 4a) based on

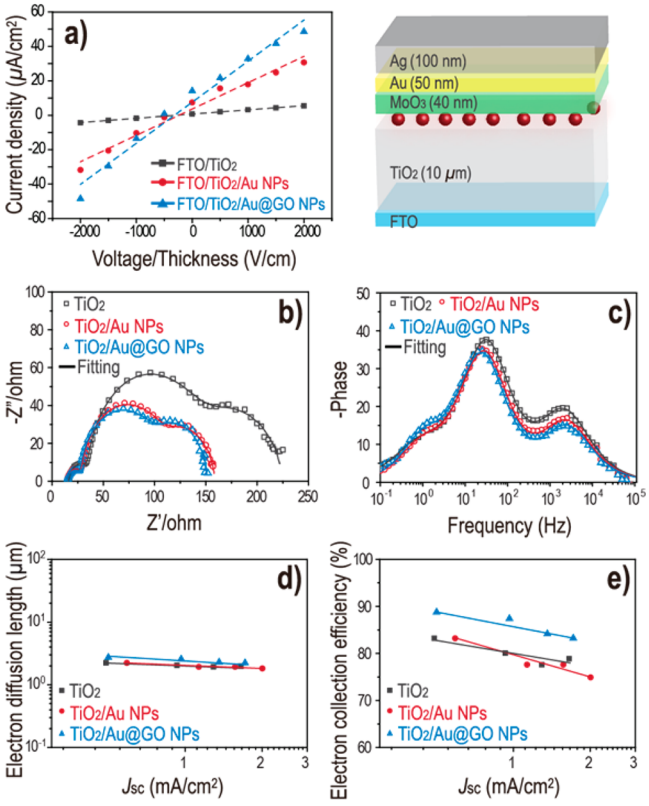

Figure 4. (a) Current density vs voltage/thickness curves with linear fitting and a schematic diagram of a symmetric film for conductivity studies. The thickness of the films was 10 μm. EIS of the control and plasmonic DSSCs with Au NPs and Au@GO NPs under the 1 sun illumination and at an open-circuit voltage: (b) Nyquist plots and (c) corresponding Bode phase plots. d) Electron diffusion length vs J_{sc} and (e) electron collection efficiency (%) vs J_{sc} of control and plasmonic DSSCs with Au and Au@GO NPs obtained from IMPS/IMVS measurements.

Ohm's law. The FTO/TiO_2/Au@GO NPs film showed the highest conductivity of 0.0238 Ω^{-1}·cm^{-1}, representing a 9.9-fold and 1.6-fold increase compared to the FTO/TiO_2 (0.0024 Ω^{-1}·cm^{-1}) and FTO/TiO_2/Au NPs (0.0153 Ω^{-1}·cm^{-1}) films, respectively. Therefore, the conductivity of the pristine TiO_2 film can be increased by incorporating plasmonic components. In addition, it is conjectured that the electrical conductivity of

DOI: 10.1021/acsenergylett.6b00612
ACS Energy Lett. 2017, 2, 117−123

the GO shell was partially recovered during the ethylenediamine-mediated functionalization process via restoration of a portion of the sp^2 bonding networks, granting a further increase in conductivity of the TiO_2 film.[40]

The electrical properties of the devices were further investigated by EIS analysis. Under 1 sun illumination and at an open-circuit voltage, the Nyquist plots (Figure 4b) and the corresponding Bode phase plots (Figure 4c) of the control and plasmonic devices were obtained from the EIS measurement. As shown in the Nyquist plots, the diameter of the semicircles in the middle frequency region, corresponding to the charge transfer resistance R_2, notably decreased in the case of plasmonic devices. The R_2 values of the control device and plasmonic devices with Au NPs and Au@GO NPs were measured to be 100, 77, and 71 Ω, respectively. The reduction of R_2 was attributed to the contribution of plasmonic Au NPs, leading to better charge separation. Furthermore, the GO shell could also effectively reduce the recombination rate by protecting the Au NPs, and as a result, the charge transfer resistance markedly decreased. The corresponding Bode phase plots to support this result are presented in Figure 4c. The electron lifetime (τ_e) can be determined from the middle frequency (f_{mid}) of the Bode phase plots with $\tau_e = 1/(2\pi f_{mid})$. The device with Au@GO NPs has the longest calculated electron lifetime (6.4 ms) compared to the device with Au NPs (5.70 ms) and the control device (5.0 ms). Au@GO NPs in DSSCs allow for longer electron transport by inhibiting the charge recombination. To further study the behavior of photoinjected charge carriers relating to charge transport and extraction, we performed IMPS and IMVS. Figure 4d,e shows the electron diffusion length (L_n) and electron collection efficiency (η_{cc}, %), respectively. Each parameter (L_n and η_{cc}) of the device with Au@GO NPs was greater than that of the others.

According to our experimental findings, the existence of a thin GO shell can improve the performance through increased charge collection in longer-wavelength ranges by GO-induced broad-band light absorption (minor possibility) and improved charge transport by enhanced electrical conductivity (major possibility), as validated by electrical measurements.

In summary, a thin layer of GO was introduced on the surface of Au NPs to demonstrate plasmon-enhanced DSSCs. The inclusion of Au@GO NPs resulted in broad absorption over the entire visible spectrum, which contributed to remarkable improvement in photocurrent generation and the performance of the fabricated solar cells. When Au@GO core−shell structures were deposited in the optimum amount, a J_{sc} of 17.2 $mA{\cdot}cm^{-2}$ and an efficiency of 9.1%, were achieved, which is superior to those of both the pristine Au plasmonic device and plasmon-free control devices. On the basis of comprehensive investigations, we concluded that a thin GO shell on Au NPs plays a significant role in enhancing the performance of DSSCs by synergistically improving light absorption and facilitating charge transport through reduction of charge recombination. DSSCs with ∼13% efficiency have been achieved by M. Grätzel's group through molecular engineering of a porphyrin dye;[41] in our study, a plasmon-mediated high-performance DSSC was proposed based on a more conventional architecture with a standard and widely available dye and electrolyte. The protocol established in this study can be employed as a generalized strategy to develop other types of high-performance solar cells.

EXPERIMENTAL METHODS

Synthesis of Gold Nanoparticles (Au NPs). Citrate-capped 55 nm diameter Au NPs were synthesized following a previously reported method.[42] An aqueous solution of 0.01 wt % chloroauric acid (200 mL) was added to a round-bottom flask and then boiled up to 130 °C using hot oil bath. Then, 1.4 mL of 1 wt % sodium citrate was quickly added to the boiled solution and stirred for 30 min, yielding a bold-pink Au NP solution.

Synthesis of Au@Graphene Oxide Nanoparticles (Au@GO NPs). Negatively charged GO (GO-COO^-) was initially prepared by the modified Hummer method.[32] To encapsulate the citrate-capped Au NPs with GO, positively charged GO (GO-NH_3^+) was prepared by attaching an amine functional group on the surface of GO-COO^-, as reported previously.[43] The as-prepared GO aqueous solution (50 mL) with negative charge was stirred for 4 h with 500 mg of EDC, 5 mL of ethylenediamine, and 1 mL of triethylamine. The as-synthesized Au NPs were centrifuged, and their precipitate was dispersed into a positively charged GO solution with the same volume, followed by gentle stirring overnight. The solution obtained was washed via centrifugation to remove the residual reactants.

Fabrication of the Plasmonic Photoanode and Devices. Glass covered with FTO (2.2 mm thick and sheet resistance of 6−9 Ohms $sq.^{-1}$) was used as the transparent conducting oxide (TCO) substrate. Before use, the FTO substrate was cleaned by sonication in acetone and isopropyl alcohol sequentially for 20 min. Commercially available TiO_2 paste (TTP-20N, ENB KOREA Co., Ltd.) was printed onto the FTO substrate by the doctor-blade method and sintered at 550 °C for 2 h to obtain a uniform TiO_2 film. To control the thickness of the TiO_2 film, three-layered 3M tape was used as a thickness guide. The thickness of the photoanodes was 11 ± 0.5 μm, as measured by the surface profiler (Alpha step). To immobilize the plasmonic NPs onto the TiO_2 film, the latter was first immersed in a 10 vol % APTES ethanolic solution. The APTES-modified TiO_2 film was then immersed in the GO-modified Au NP colloidal solution with different dipping time (30, 60, and 180 min), followed by DI washing and drying with nitrogen. Finally, ruthenium dye (*cis*-diisothiocyanato-bis(2,2′-bipyridyl-4,4′-dicarboxylato) ruthenium(II) bis(tetrabutylammonium), N-719, Solaronix) was sensitized on the TiO_2/Au@GO NPs film to constitute the plasmonic photoanode by immersing into dye solution (5 mM in ethanol) for 24 h. The plasmonic photoanode was assembled with Pt-coated FTO as the counter electrode using a 50 μm thick hot-melt spacer (SX1170-25, Solaronix), and an ionic liquid electrolyte, 0.60 M BMIM-I, 0.03 M I_2, 0.50 M TBP, and 0.10 M GTC in acetonitrile/valeronitrile 85/15 (v/v) (no. ES-0004), purchased from io.li.tec (Germany), was then injected between the two electrodes through capillary force.

Electromagnetic Simulation. For the electromagnetic simulation of Au and Au@GO NPs, a three-dimensional FDTD method was used. The absorption spectrum was obtained from near-field calculation, in which the total absorbed power was calculated from eq 1

$$P_{abs} = \frac{\omega}{2}\int_v \mathrm{Im}[\varepsilon(\omega)]|\mathbf{E}|^2\,\mathrm{d}v \quad (1)$$

where ω is the frequency of the incident radiation, ε is the permittivity of the medium, and $\mathbf{E}$ is the electric field amplitude. For the absorption simulation, symmetry boundary conditions

DOI: 10.1021/acsenergylett.6b00612
ACS Energy Lett. 2017, 2, 117−123

were imposed at the center of NPs in the *yz* and *zx* planes with a linearly polarized plane wave incident along the *z* direction. The grid size was set to 2 and 1 nm^3 for the Au NP and Au@GO NP, respectively. The near-field distribution was obtained without symmetry boundary conditions, in which case the grid size was set to 1 nm^3 for both the Au NP and Au@GO NP. A perfectly matched layer with 10 nm width was used for the entire simulation. The refractive indices of Au and GO were taken from the literature.[44,45]

Conductivity Measurement and Calculation. For the conductivity measurement, the electrode layers, consisting of ∼40 nm of thermally evaporated molybdenum oxide, ∼50 nm of electron-beam-deposited gold, and ∼100 nm of thermally evaporated silver (MoO_3/Au/Ag), were deposited on top of the photoanode films using an Angstrom Engineering Åmod deposition system in an Innovative Technology glovebox. Current−voltage characteristics in dark conditions were measured using a Keithley 2400 source meter. Conductivity calculation is based on eq 2 (Ohm's law)

$$J = \sigma \frac{V}{d} \tag{2}$$

where J is the current density ($mA \cdot cm^{-2}$), σ is the conductivity ($\Omega^{-1} \cdot cm^{-1}$), V is the applied voltage (V), and d is the thickness of the TiO_2 or TiO_2/Au NPs or the TiO_2/Au@GO NP films on the FTO substrate (10 μm).

Characterization of Materials and Device Performance. The amine functionalization of GO (GO-NH_3^+) was shown using an XPS (ESCALab spectrometer (Thermo VG, U.K.) equipped with monochromated Al−Kα radiation) and ζ-potential measurement (ZETASIZER 3000, Malvern). To characterize the GO shell on Au NPs, Raman spectroscopy was performed using a LabRam HREvo 800 (HORIBA Jobin Yvon) at an excitation wavelength of 633 nm. The structure of the Au@GO NPs was thoroughly examined by transmission electron microscopy (TEM, JEOL JSM2100-F, at 100 kV). The optical properties were measured by UV−vis absorption spectroscopy (Cary 5000, Varian Inc.). Photocurrent−voltage (J−V) curves and EIS were measured under a simulated AM 1.5 G illumination intensity of 100 mA cm^{-2} (Polaronix K201, McScience Inc.) using an electrochemical measurement system (InviumStat.XR, Invium Technologies). EIS measurement was performed by applying a 20 mV AC signal in the range of frequency from 50 mHz to 10 kHz. For IMPS/IMVS measurements, a green-light-emitting diode (525 nm) was used as the light source, and its intensity was modulated using a sinewave generator with the frequency set from 0.1 to 100 Hz (Invium ModuLight-module, Invium Technologies). SKPM measurement was carried out using a KPTechnology KP020 system. The work functions of the photoanode films were measured sequentially in the dark and under xenon light illumination (770 $W \cdot cm^{-2}$) for 380 s at each step.

■ ASSOCIATED CONTENT

Supporting Information

The Supporting Information is available free of charge on the ACS Publications website at DOI: 10.1021/acsenergylett.6b00612.

Characterizations of positively charged graphene oxide and Au NPs and additional J−V curves and photovoltaic parameters of plasmonic DSSCs with varying amounts of Au and Au@GO NPs (PDF)

■ AUTHOR INFORMATION

Corresponding Authors

*E-mail: dhkim@ewha.ac.kr (D.H.K.).
*E-mail: ted.sargent@utoronto.ca (E.H.S.).

ORCID

Olivier Ouellette: 0000-0001-5708-5058
Dong Ha Kim: 0000-0003-0444-0479

Present Addresses

‖Y.H.J.: Photo-Electronic Hybrids Research Center, Korea Institute of Science and Technology (KIST), 5, Hwarang-ro, 14-gil, Seongbuk-gu, Seoul, 02792, South Korea.
#P.K.: Material Science and Engineering, Mahidol University, 272 Rama 6 Rd., Ratchathewi District, Bangkok, 10400, Thailand.

Notes

The authors declare no competing financial interest.

■ ACKNOWLEDGMENTS

This study was supported by the National Research Foundation of Korea Grant funded by the Korean Government (2014R1A2A1A09005656, 2015M1A2A2058365, 2011-0030255). T.S. and D.K. acknowledge support by the National Research Foundation (NRF) grants funded by the Korean Government (2015R1A2A1A10052826). O. Ouellette was financially supported by NSERC's CREATE Program in Materials for Enhanced Energy Technologies.

■ REFERENCES

(1) Atwater, H. A.; Polman, A. Plasmonics for Improved Photovoltaic Devices. *Nat. Mater.* **2010**, *9*, 205−213.
(2) Ferry, V. E.; Munday, J. N.; Atwater, H. A. Design Considerations for Plasmonic Photovoltaics. *Adv. Mater.* **2010**, *22*, 4794−4808.
(3) Spinelli, P.; Ferry, V.; Van De Groep, J.; Van Lare, M.; Verschuuren, M.; Schropp, R.; Atwater, H.; Polman, A. Plasmonic Light Trapping in Thin-Film Si Solar Cells. *J. Opt.* **2012**, *14*, 024002.
(4) Fei Guo, C.; Sun, T.; Cao, F.; Liu, Q.; Ren, Z. Metallic Nanostructures for Light Trapping in Energy-Harvesting Devices. *Light: Sci. Appl.* **2014**, *3*, e161.
(5) Pillai, S.; Green, M. Plasmonics for Photovoltaic Applications. *Sol. Energy Mater. Sol. Cells* **2010**, *94*, 1481−1486.
(6) Gan, Q.; Bartoli, F. J.; Kafafi, Z. H. Plasmonic-Enhanced Organic Photovoltaics: Breaking the 10% Efficiency Barrier. *Adv. Mater.* **2013**, *25*, 2385−2396.
(7) Brown, M. D.; Suteewong, T.; Kumar, R. S. S.; D'Innocenzo, V.; Petrozza, A.; Lee, M. M.; Wiesner, U.; Snaith, H. J. Plasmonic Dye-Sensitized Solar Cells Using Core-Shell Metal-Insulator Nanoparticles. *Nano Lett.* **2011**, *11*, 438−445.
(8) Standridge, S. D.; Schatz, G. C.; Hupp, J. T. Distance Dependence of Plasmon-Enhanced Photocurrent in Dye-Sensitized Solar Cells. *J. Am. Chem. Soc.* **2009**, *131*, 8407−8409.
(9) Yang, J.; You, J.; Chen, C.-C.; Hsu, W.-C.; Tan, H.-r.; Zhang, X. W.; Hong, Z.; Yang, Y. Plasmonic Polymer Tandem Solar Cell. *ACS Nano* **2011**, *5*, 6210−6217.
(10) Wang, D. H.; Kim, D. Y.; Choi, K. W.; Seo, J. H.; Im, S. H.; Park, J. H.; Park, O. O.; Heeger, A. J. Enhancement of Donor−Acceptor Polymer Bulk Heterojunction Solar Cell Power Conversion Efficiencies by Addition of Au Nanoparticles. *Angew. Chem.* **2011**, *123*, 5633−5637.
(11) Catchpole, K.; Polman, A. Plasmonic Solar Cells. *Opt. Express* **2008**, *16*, 21793−21800.
(12) Ferry, V. E.; Sweatlock, L. A.; Pacifici, D.; Atwater, H. A. Plasmonic Nanostructure Design for Efficient Light Coupling into Solar Cells. *Nano Lett.* **2008**, *8*, 4391−4397.

DOI: 10.1021/acsenergylett.6b00612
ACS Energy Lett. 2017, 2, 117−123

(13) Tan, H.; Santbergen, R.; Smets, A. H.; Zeman, M. Plasmonic Light Trapping in Thin-Film Silicon Solar Cells with Improved Self-Assembled Silver Nanoparticles. *Nano Lett.* **2012**, *12*, 4070−4076.
(14) Ding, I.; Zhu, J.; Cai, W.; Moon, S. J.; Cai, N.; Wang, P.; Zakeeruddin, S. M.; Grätzel, M.; Brongersma, M. L.; Cui, Y.; et al. Plasmonic Dye-Sensitized Solar Cells. *Adv. Energy Mater.* **2011**, *1*, 52−57.
(15) Reineck, P.; Lee, G. P.; Brick, D.; Karg, M.; Mulvaney, P.; Bach, U. A Solid-State Plasmonic Solar Cell via Metal Nanoparticle Self-Assembly. *Adv. Mater.* **2012**, *24*, 4750−4755.
(16) Su, Y.-H.; Ke, Y.-F.; Cai, S.-L.; Yao, Q.-Y. Surface Plasmon Resonance of Layer-by-Layer Gold Nanoparticles Induced Photoelectric Current in Environmentally-Friendly Plasmon-Sensitized Solar Cell. *Light: Sci. Appl.* **2012**, *1*, e14.
(17) Zhang, W.; Saliba, M.; Stranks, S. D.; Sun, Y.; Shi, X.; Wiesner, U.; Snaith, H. J. Enhancement of Perovskite-Based Solar Cells Employing Core-Shell Metal Nanoparticles. *Nano Lett.* **2013**, *13*, 4505−4510.
(18) Ding, B.; Lee, B. J.; Yang, M.; Jung, H. S.; Lee, J. K. Surface-Plasmon Assisted Energy Conversion in Dye-Sensitized Solar Cells. *Adv. Energy Mater.* **2011**, *1*, 415−421.
(19) Choi, H.; Chen, W. T.; Kamat, P. V. *Know Thy Nano Neighbor*. Plasmonic *versus* Electron Charging Effects of Metal Nanoparticles in Dye-Sensitized Solar Cells. *ACS Nano* **2012**, *6*, 4418−4427.
(20) Wen, C.; Ishikawa, K.; Kishima, M.; Yamada, K. Effects of Silver Particles on the Photovoltaic Properties of Dye-Sensitized TiO_2 Thin Films. *Sol. Energy Mater. Sol. Cells* **2000**, *61*, 339−351.
(21) Hägglund, C.; Zäch, M.; Kasemo, B. Enhanced Charge Carrier Generation in Dye Sensitized Solar Cells by Nanoparticle Plasmons. *Appl. Phys. Lett.* **2008**, *92*, 013113.
(22) Li, Y.; Wang, H.; Feng, Q.; Zhou, G.; Wang, Z.-S. Gold Nanoparticles Inlaid TiO_2 Photoanodes: A Superior Candidate for High-Efficiency Dye-Sensitized Solar Cells. *Energy Environ. Sci.* **2013**, *6*, 2156−2165.
(23) Dang, X.; Qi, J.; Klug, M. T.; Chen, P.-Y.; Yun, D. S.; Fang, N. X.; Hammond, P. T.; Belcher, A. M. Tunable Localized Surface Plasmon-Enabled Broadband Light-Harvesting Enhancement for High-Efficiency Panchromatic Dye-Sensitized Solar Cells. *Nano Lett.* **2013**, *13*, 637−642.
(24) Du, J.; Qi, J.; Wang, D.; Tang, Z. Facile Synthesis of Au@TiO_2 Core-Shell Hollow Spheres for Dye-Sensitized Solar Cells with Remarkably Improved Efficiency. *Energy Environ. Sci.* **2012**, *5*, 6914−6918.
(25) Jang, Y. H.; Jang, Y. J.; Kochuveedu, S. T.; Byun, M.; Lin, Z.; Kim, D. H. Plasmonic Dye-Sensitized Solar Cells Incorporated with Au−TiO_2 Nanostructures with Tailored Configurations. *Nanoscale* **2014**, *6*, 1823−1832.
(26) Zarick, H. F.; Hurd, O.; Webb, J. A.; Hungerford, C.; Erwin, W. R.; Bardhan, R. Enhanced Efficiency in Dye-Sensitized Solar Cells with Shape-Controlled Plasmonic Nanostructures. *ACS Photonics* **2014**, *1*, 806−811.
(27) Kim, S. R.; Parvez, M. K.; Chhowalla, M. UV-reduction of graphene oxide and its application as an interfacial layer to reduce the back-transport reactions in dye-sensitized solar cells. *Chem. Phys. Lett.* **2009**, *483*, 124−127.
(28) Yang, N.; Zhai, J.; Wang, D.; Chen, Y.; Jiang, L. Two-dimensional graphene bridges enhanced photoinduced charge transport in dye-sensitized solar cells. *ACS Nano* **2010**, *4*, 887−894.
(29) Yang, D.; Zhou, L.; Chen, L.; Zhao, B.; Zhang, J.; Li, C. Chemically modified graphene oxides as a hole transport layer in organic solar cells. *Chem. Commun.* **2012**, *48*, 8078−8080.
(30) Wang, J. T.-W.; Ball, J. M.; Barea, E. M.; Abate, A.; Alexander-Webber, J. A.; Huang, J.; Saliba, M.; Mora-Sero, I. n.; Bisquert, J.; Snaith, H. J.; et al. Low-temperature processed electron collection layers of graphene/TiO2 nanocomposites in thin film perovskite solar cells. *Nano Lett.* **2014**, *14*, 724−730.
(31) Konios, D.; Kakavelakis, G.; Petridis, C.; Savva, K.; Stratakis, E.; Kymakis, E. Highly efficient organic photovoltaic devices utilizing work-function tuned graphene oxide derivatives as the anode and cathode charge extraction layers. *J. Mater. Chem. A* **2016**, *4*, 1612−1623.
(32) Hummers, W. S., Jr; Offeman, R. E. Preparation of Graphitic Oxide. *J. Am. Chem. Soc.* **1958**, *80*, 1339−1339.
(33) Meng, D.; Yang, S.; Sun, D.; Zeng, Y.; Sun, J.; Li, Y.; Yan, S.; Huang, Y.; Bielawski, C. W.; Geng, J. A Dual-Fluorescent Composite of Graphene Oxide And Poly(3-Hexylthiophene) Enables The Ratiometric Detection of Amines. *Chem. Sci.* **2014**, *5*, 3130−3134.
(34) Zhu, H.; Gao, L.; Jiang, X.; Liu, R.; Wei, Y.; Wang, Y.; Zhao, Y.; Chai, Z.; Gao, X. Positively Charged Graphene Oxide Nanoparticle: Precisely Label the Plasma Membrane of Live Cell and Sensitively Monitor Extracellular pH *In Situ*. *Chem. Commun.* **2014**, *50*, 3695−3698.
(35) Huang, P.; Xu, C.; Lin, J.; Wang, C.; Wang, X.; Zhang, C.; Zhou, X.; Guo, S.; Cui, D. Folic Acid-Conjugated Graphene Oxide Loaded with Photosensitizers for Targeting Photodynamic Therapy. *Theranostics* **2011**, *1*, 240.
(36) Tuinstra, F.; Koenig, J. L. Raman Spectrum of Graphite. *J. Chem. Phys.* **1970**, *53*, 1126−1130.
(37) Ferrari, A. C.; Basko, D. M. Raman spectroscopy as a versatile tool for studying the properties of graphene. *Nat. Nanotechnol.* **2013**, *8*, 235−246.
(38) Wang, P.; Liu, Z.-G.; Chen, X.; Meng, F.-L.; Liu, J.-H.; Huang, X.-J. UV irradiation synthesis of an Au−graphene nanocomposite with enhanced electrochemical sensing properties. *J. Mater. Chem. A* **2013**, *1*, 9189−9195.
(39) Yuan, Z.; Wu, Z.; Bai, S.; Xia, Z.; Xu, W.; Song, T.; Wu, H.; Xu, L.; Si, J.; Jin, Y. Hot-Electron Injection in a Sandwiched TiO_x−Au−TiO_x Structure for High-Performance Planar Perovskite Solar Cells. *Adv. Energy Mater.* **2015**, *5*, 1500038.
(40) Hu, H.; Zhao, Z.; Wan, W.; Gogotsi, Y.; Qiu, J. Ultralight and Highly Compressible Graphene Aerogels. *Adv. Mater.* **2013**, *25*, 2219−2223.
(41) Mathew, S.; Yella, A.; Gao, P.; Humphry-Baker, R.; Curchod, B. F.; Ashari-Astani, N.; Tavernelli, I.; Rothlisberger, U.; Nazeeruddin, M. K.; Grätzel, M. Dye-sensitized solar cells with 13% efficiency achieved through the molecular engineering of porphyrin sensitizers. *Nat. Chem.* **2014**, *6*, 242−247.
(42) Li, J. F.; Tian, X. D.; Li, S. B.; Anema, J. R.; Yang, Z. L.; Ding, Y.; Wu, Y. F.; Zeng, Y. M.; Chen, Q. Z.; Ren, B.; et al. Surface Analysis Using Shell-Isolated Nanoparticle-Enhanced Raman Spectroscopy. *Nat. Protoc.* **2012**, *8*, 52−65.
(43) Hong, J.; Char, K.; Kim, B.-S. Hollow Capsules of Reduced Graphene Oxide Nanosheets Assembled on a Sacrificial Colloidal Particle. *J. Phys. Chem. Lett.* **2010**, *1*, 3442−3445.
(44) Palik, E. D. *Handbook of Optical Constants of Solids: Index*; Elsevier, 1998; Vol. 3.
(45) Jung, I.; Vaupel, M.; Pelton, M.; Piner, R.; Dikin, D. A.; Stankovich, S.; An, J.; Ruoff, R. S. Characterization of Thermally Reduced Graphene Oxide by Imaging Ellipsometry. *J. Phys. Chem. C* **2008**, *112*, 8499−8506.

DOI: 10.1021/acsenergylett.6b00612
ACS Energy Lett. 2017, 2, 117−123